Research Square

Preprints are preliminary reports that have not undergone peer review.
They should not be considered conclusive, used to inform clinical practice,
or referenced by the media as validated information.

Quantum Geometric Injection and Shift Optical Forces Drive Coherent Phonons

J. Luke Pimlott
University of Bath
Habib Rostami
hr745@bath.ac.uk
University of Bath

Article

Keywords:

Posted Date: November 24th, 2026

DOI: https://doi.org/10.21203/rs.3.rs-11457341/v1

License: This work is licensed under a Creative Commons Attribution 4.0 International License.
Read Full License

Additional Declarations: No competing interests reported.

Quantum Geometric Injection and Shift Optical Forces Drive Coherent Phonons

J. Luke Pimlott[1,*] and Habib Rostami[1,†]

[1] *Department of Physics, University of Bath, Claverton Down, Bath BA2 7AY, United Kingdom*

We develop a gauge-invariant quantum-geometric theory of light-induced Raman forces driving coherent lattice dynamics in solids. We show that the resonant interband response separates into injection and shift forces, providing the lattice analogue of injection and shift photocurrents. Crucially, the electronic quantum metric and Berry curvature directly govern these forces, weighted by distinct electron–phonon quantities. The injection force is controlled by the quantum geometric tensor and differences between band-diagonal electron–phonon couplings, producing the resonant displacive response. The shift force is a resonant impulsive response governed by quantum geometry and a phononic shift vector arising from interband electron–phonon coherence. We derive polarization selection rules, symmetry constraints, and temporal signatures. The interplay of impulsive shift and displacive injection forces acting along perpendicular directions enables chiral phonon motion under linearly polarised optical excitation. Applied to interlayer shear phonons in a bilayer Haldane model, the theory predicts tunability with optical frequency, topology, electronic temperature, and current-induced symmetry breaking. These results establish a quantum-geometric framework for coherent lattice dynamics and identify coherent phonons as experimentally accessible signatures of electronic quantum geometry in quantum materials.

INTRODUCTION

Coherent optical manipulation of quantum materials involves light-induced forces that act by exciting lattice vibration modes. These drive ultrafast phase transitions to transient phases, such as from a normal metal to a topological insulator, or to superconducting, ferroelectric, or ferromagnetic phases [1–5], and impact nonlinear photocurrent generation [6, 7]. Coherent excitation of Raman-active phonons is driven by light-induced *Raman forces* through *impulsive* or *displacive* mechanisms [8–15], enabling ultrafast non-thermal control of quantum materials. In the impulsive mechanism, ions vibrate coherently around their equilibrium positions, typical in the transparent regime. In contrast, the displacive mechanism, prevalent in the absorbing regime, involves ion displacement to new equilibrium positions.

In this work, we develop a general theory of the rectified Raman force and show that its distinct components are governed by the quantum geometry of the electronic states, encoded in the *quantum geometric tensor* (QGT) [16–18]. The band-resolved QGT is defined as

$$Q^{mn}_{ab} = g^{mn}_{ab} - \frac{i}{2}\Omega^{mn}_{ab}, \tag{1}$$

where m and n denote electronic bands, and a and b label Cartesian directions. The real part, g^{mn}_{ab}, is the band-resolved *quantum metric*, while $\Omega^{mn}_{ab} = -2\mathrm{Im}[Q^{mn}_{ab}]$ corresponds to the band-resolved *Berry curvature*.

Quantum-geometric effects have been extensively studied in contexts such as the anomalous Hall effect [19], flat-band superfluidity [18, 20], nonlinear photocurrents [21–24], nonlinear Hall effects in $\mathcal{PT}$-symmetric antiferromagnets [25–27], and electron–phonon coupling [28–31]. Despite this progress, it remains unresolved how electronic quantum geometry governs the light-induced Raman forces that generate coherent phonons capable of driving nonequilibrium phase transitions, and whether these forces decompose into distinct microscopic and temporal mechanisms. Conventional theories of coherent-phonon generation [12] are formulated primarily in terms of dielectric response and electron–phonon coupling (EPC), and do not expose the underlying quantum-geometric structure of the Raman-force response.

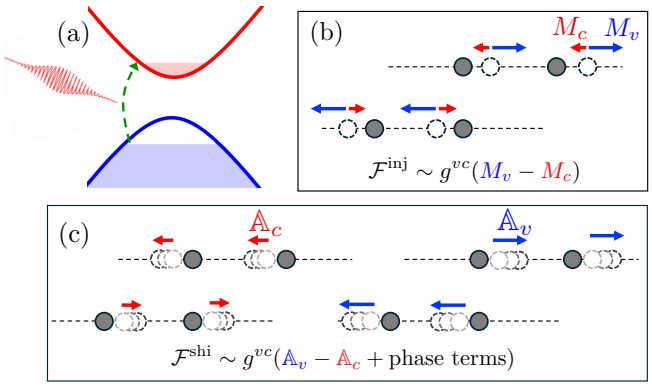

FIG. 1. (a) Light-driven interband transitions generate a Raman force (RF) in layered materials via electron–phonon coupling (EPC). (b) Injection (displacive) force arises from the difference in EPC-induced atomic forces between two bands. (c) Shift (impulsive) force arises from a gauge-invariant geometric shift in phonon conjugate momentum generated by interband coherence.

Here, we present a quantum-geometric framework for unconventional light-induced atomic forces, introducing the terms *injection force* and *shift force* by analogy with established second-order photocurrent processes [32]. We

* jlp62@bath.ac.uk
† hr745@bath.ac.uk

show that, within the clean, noninteracting limit of the electron-mediated Raman response considered here, the injection force is the sole displacive component and arises only in the absorbing (resonant) regime, where it is governed by the QGT and weighted by the mismatch in EPC strength between optically-connected bands (Fig. 1a). It therefore originates from the distinct atomic forces exerted on ions by photoexcited electrons in each band (Fig. 1b), analogous to how the injection current depends on the difference in electron group velocities between bands [32].

The shift force, meanwhile, acts as an unconventional resonant impulsive force in the absorbing regime, unlike the conventional impulsive force which typically arises in the transparent (off-resonant) regime. We formulate the shift force in terms of the QGT and a *phononic shift vector*, which quantifies the gauge-invariant geometric shift in the momentum conjugate to the phonon coordinate during an interband optical transition (Fig. 1c). This is the phononic analogue of the electronic shift vector underlying the shift current, which describes the non-diffusive real-space displacement of an electron wavepacket during an interband transition [32, 33]. This parameter is defined via the *Mead–Truhlar connection* [34, 35]: an emergent gauge field over the atomic displacement manifold, generated by the adiabatic evolution of the electronic states. It acts as an effective vector potential on phonons (shifting canonical phonon momentum $\mathbf{P} \to \mathbf{P} - \hbar\mathbb{A}$) due to electron-phonon interactions.

We apply the general quantum-geometric theory of Raman forces to quantify the forces associated with the coherent excitation of interlayer shear phonons [36–39], which correspond to the out-of-phase sliding of atomic layers in van der Waals materials. Such coherent phonon excitation is central to optically controlling stacking order in layered materials like bilayer and trilayer graphene [40] and transition metal dichalcogenides (TMDs) such as MoS_2, WSe_2, $MoTe_2$, and WTe_2 [3, 41, 42], driven by ultrashort, intense laser pulses. The coherent dynamics of shear phonons play a key role in light-induced switching of electronic topology [3, 43] and magnetism [43], modulation of Kondo screening in heterobilayers [44], and control of interlayer ferroelectric polarization in h-BN [45, 46], and TMDs [47, 48]. These effects have applications in field-effect transistors and ferroelectric memory devices [49] and offer a promising route for controlling superconducting transitions in twisted moiré graphene systems [50].

RESULTS AND DISCUSSION

Raman-force rectification: photogalvanic analogy

Light-induced Raman force is a second-order response to the incident light field $\mathbf{E}(t)$:

$$\mathcal{F}_a(\omega_\Sigma) = \int \frac{d\omega}{2\pi} \chi_{abc}(\omega, \omega_\Sigma - \omega) E^b(\omega) E^c(\omega_\Sigma - \omega), \quad (2)$$

assuming the Einstein convention for summation on the repeated Cartesian indices, and with χ_{abc} the Raman-force response function, which is the correlation of EPC with light-matter couplings.

The rectified Raman-force response $\chi_{abc}(\omega, -\omega)$ was previously shown to describe rigid atomic displacement and phonon splitting and softening under monochromatic driving [14, 15]. Those works, however, did not identify the resonant response in terms of distinct injection and shift mechanisms, nor formulate their quantum-geometric structure or contrasting temporal dynamics under pulsed excitation.

Using the Kadanoff–Baym formalism, we derive the complete Raman-force susceptibility in Supplementary Note 1. The resulting diagrams are evaluated explicitly in the band basis in Supplementary Note 2 (see also Methods). We show that the Raman-force response separates into resonant injection and shift channels, together with an off-resonant contribution. Under pulsed excitation, the injection channel contains both a singular term leading to a displacive response and a regular term with impulsive character, whereas the shift force is intrinsically regular and impulsive. In the nearly-rectified regime ($\hbar|\omega_\Sigma| \ll \varepsilon_g$, with ε_g the band gap), the susceptibility separates into a pole and a regular part:

$$\chi_{abc}(\omega, \omega_\Sigma - \omega) = \frac{\alpha_{abc}(\omega)}{i\omega_\Sigma} + \beta_{abc}(\omega) + \mathcal{O}(\omega_\Sigma). \quad (3)$$

The first term has a pole at $\omega_\Sigma = 0$, describing a force that accumulates under illumination in the absence of relaxation. The force-generation rate $d\mathcal{F}/dt$ nevertheless remains finite, analogous to the *injection photocurrent* [32, 51]. We therefore call this contribution the *injection force*, denote its coefficient by $\alpha^{\text{inj}}_{abc}(\omega) \equiv \alpha_{abc}(\omega)$, and show below that it produces a displacive lattice response. The regular part is analytic in ω_Σ and approaches $\beta_{abc}(\omega)$ as $\omega_\Sigma \to 0$. It comprises three contributions:

$$\beta_{abc}(\omega) = \beta^{\text{reg-inj}}_{abc}(\omega) + \beta^{\text{shi}}_{abc}(\omega) + \beta^{\text{off}}_{abc}(\omega). \quad (4)$$

The first is a resonant term, $\beta^{\text{reg-inj}}_{abc} = (i/2)\partial_\omega \alpha^{\text{inj}}_{abc}(\omega)$, which we call the *regular injection* response. The second, also resonant, is governed by a phononic shift vector, as shown below; we call it the *shift force* by analogy with the shift photocurrent. The third collects all off-resonant contributions.

We focus here on the resonant forces, deferring the off-resonant response to the Supplementary Material. In the

time domain, the injection, regular injection, and shift forces take the form

$$\mathcal{F}_a^{\rm inj}(t) = -\int_{-\infty}^{t} dt' \int dt''\, \widetilde{\alpha}^{\rm inj}_{abc}(t'') E^b(t'-t'') E^c(t') e^{\Gamma(t'-t)},$$
$$\mathcal{F}_a^{\rm shi+reg}(t) = \int dt' \left[\widetilde{\beta}^{\rm shi}_{abc}(t') - \frac{t'}{2}\widetilde{\alpha}^{\rm inj}_{abc}(t')\right] E^b(t-t') E^c(t), \tag{5}$$

where Γ is the electronic relaxation rate. All integrals extend over the real axis, and tildes denote inverse Fourier transforms with respect to the optical frequency. For a Gaussian pulse, $\mathbf{E}(t) = \mathbf{E}_0 \cos(\omega_0 t) e^{-t^2/(2\sigma^2)}$, the singular injection contribution accumulates during excitation and relaxes on the timescale Γ^{-1}, producing a long-lived displacive response. The regular injection term provides an impulsive correction during the pulse, governed by the spectral dispersion of $\alpha^{\rm inj}$. The shift force is also impulsive but arises from a distinct mechanism involving interband electronic coherence. For frequency-independent $\alpha^{\rm inj}_{abc}$, the regular injection correction vanishes, and $\mathcal{F}_a^{\rm inj}(t) = -\alpha^{\rm inj}_{abc} \int_{-\infty}^{t} dt'\, e^{-\Gamma(t-t')} E^b(t') E^c(t')$. Likewise, frequency-independent $\beta^{\rm shi}_{abc}$ gives $\mathcal{F}_a^{\rm shi}(t) = \beta^{\rm shi}_{abc} E^b(t) E^c(t)$. For fixed polarization, these forces follow the accumulated and instantaneous pulse intensity, respectively, reproducing the conventional displacive and impulsive temporal profiles [12]. Using the frequency-dependent Raman response tensors of Eqs. (23) and (24), we compute the real-time resonant Raman driving force via Eq. (5) and obtain the lattice displacement, $u(t)$ shown in Fig. 2 by solving

$$\ddot{u}(t) + 2\gamma_p \dot{u}(t) + \omega_p^2 u(t) = \mathcal{F}(t)/\rho, \tag{6}$$

where ρ is the mass density, ω_p the phonon frequency, and γ_p the phonon decay rate. The injection term $\alpha^{\rm inj}_{abc}$ produces a *displacive* force that, in the clean limit ($\Gamma \to 0$), approaches a finite constant after the pulse, whereas for finite electronic relaxation it decays on the timescale Γ^{-1}. In contrast, the shift term $\beta^{\rm shi}_{abc}$ and the regular injection term $\beta^{\rm reg\text{-}inj}_{abc}$ generate *impulsive* forces confined to the pulse duration and independent of Γ at this order. This distinction in the force profiles translates directly into the coherent phonon dynamics: the numerical results reveal an almost $\pi/2$ phase difference between the oscillations generated by the injection and shift forces, consistent with the ideal cosine- and sine-like responses expected for displacive and impulsive excitation, respectively [11, 12].

This temporal structure closely parallels that of injection and shift photocurrents driven by an ultrashort pulse [52]. In particular, disorder scattering at rate Γ causes the injection contribution to relax, while the shift contribution remains localized to the optical excitation and does not develop an injection-like relaxation tail, reflecting the same non-diffusive character as the *shift photocurrent* [32]. Table I summarizes this correspondence between injection and shift mechanisms in photocurrents and Raman forces. This analogy, in turn, motivates extending the quantum-geometric description developed for photocurrents [22, 23] to Raman forces.

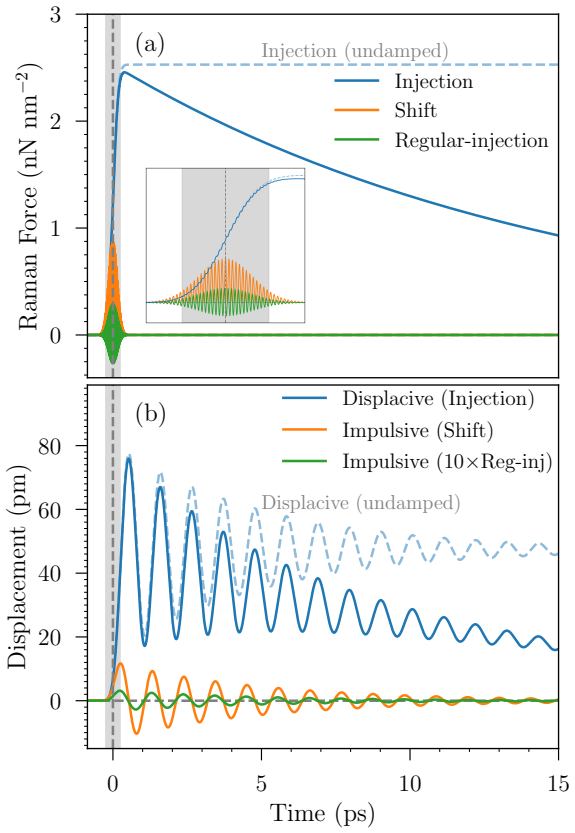

FIG. 2. Resonant Raman forces and phonon dynamics. (a) Injection, shift, and regular injection forces calculated from Eq. (5) and Eqs. (23)–(24) for a Gaussian pulse $E(t) = E_0 \cos(\omega_0 t) e^{-t^2/(2\sigma^2)}$, with $E_0 \approx 100$ MV/m, $\sigma = 200$ fs, $\hbar\omega_0 = 2.2\delta_{\rm H}$, Haldane gap, $\delta_{\rm H} = 50$ meV, and $\tau = \Gamma^{-1} = 15$ ps. Gray shading indicates the pulse width; the inset resolves the forces during the pulse. (b) Shear-phonon displacements driven separately by the injection (displacive), shift (impulsive), and regular injection (impulsive) forces, with phonon energy $\hbar\omega_p = 3.9$ meV, lifetime $\tau_p = \gamma_p^{-1} = 5$ ps, and areal mass density $\rho \approx 1.5$ mg/m^2. The regular injection displacement is magnified by a factor of ten. Dashed curves show the injection response in the clean limit ($\Gamma \to 0$); the shift and regular injection responses are independent of Γ at this order.

In Supplementary Note 3, we develop the quantum-geometric formulation of the resonant injection and shift forces. The resonant response separates into a band-diagonal injection channel, containing both the singular population pole and its regular finite-bandwidth correction, and an interband-coherence channel underlying the shift force. The cancellation of the remaining resonant counterterms is demonstrated in Supplementary Note 4, while the complete off-resonant response, consisting of three distinct contributions, is derived and numerically analyzed in Supplementary Note 5. Hereafter, we focus

TABLE I. Analogy between coherent photocurrent and coherent Raman force in the rectified ($\omega_\Sigma \approx 0$) sector of the second-order response. Here $I(t) \propto |\mathbf{E}(t)|^2$ is the pulse intensity envelope, and $\tau = 1/\Gamma$ is the electronic relaxation time. Here we compare the conventional singular injection response; the regular injection term arising from the finite-bandwidth correction is not included in the photocurrent comparison.

Type	Regime	Photocurrent	Raman force (this work)
Injection	clean limit	$J(\omega_\Sigma \to 0) \sim 1/(i\omega_\Sigma)$ (singular) [32]	$\mathcal{F}(\omega_\Sigma \to 0) \sim 1/(i\omega_\Sigma)$ (singular)
	monochromatic	$J \propto \tau\times$ interband velocity asymm. [22, 51]	$\mathcal{F} \propto \tau\times$ interband EPC asymm.
	pulsed	long-lived (memoryful), relaxation-limited [52]	displacive: $\mathcal{F}(t) \propto \int_{-\infty}^{t} dt'\, I(t')\, e^{(t'-t)/\tau}$
Shift	clean limit	$J(\omega_\Sigma \to 0) = \text{const.}$ [32, 53]	$\mathcal{F}(\omega_\Sigma \to 0) = \text{const.}$
	monochromatic	$J \propto$ electronic shift vector, τ-indep. [32, 53]	$\mathcal{F} \propto$ phononic shift vector, τ-indep.
	pulsed	instantaneous (memoryless), τ-indep. [52, 54]	impulsive: $\mathcal{F}(t) \propto I(t)$ (vanishes after pulse)

on the resonant injection and shift Raman-force channels and their quantum-geometric structure under linearly and circularly polarized optical excitation.

Quantum-geometric injection and shift forces

For linearly polarized (LP) excitation, the injection and shift forces can be expressed in terms of the quantum metric as (see Supplementary Note 3)

$$\begin{bmatrix} \alpha^{\text{inj-LP}}_{abb}(\omega) \\ \beta^{\text{shi-LP}}_{abb}(\omega) \end{bmatrix} = \frac{g_s \pi e^2}{\hbar} \sum_{\mathbf{p}} \sum_{mn} f_{mn} g^{nm}_{bb} \begin{bmatrix} \frac{\Delta^{nm}_a}{\hbar} \\ \mathbb{R}^{mn}_{a;b} \end{bmatrix} \delta(\omega - \omega_{nm}) \tag{7}$$

with spin degeneracy factor $g_s = 2$. Here, the band-resolved quantum metric reads

$$g^{nm}_{bc} = \text{Re}[\mathcal{A}^{nm}_b \mathcal{A}^{mn}_c], \tag{8}$$

with $\mathcal{A}^{nm}_b = i\hbar\langle\phi_n|\partial_{p_b}\phi_m\rangle$ the Berry connection and $|\phi_n\rangle$ the Bloch state of band n. Additionally,

$$\Delta^{mn}_a = \langle\phi_m|\hat{M}_a|\phi_m\rangle - \langle\phi_n|\hat{M}_a|\phi_n\rangle = [\partial_{u_a}\varepsilon_{mn}]_{\mathbf{u}\to 0} \tag{9}$$

is the EPC-difference between bands, $\hbar\omega_{mn} = \varepsilon_{mn} = \varepsilon_m - \varepsilon_n$, and $f_{mn} = f_m - f_n$, with f_n the Fermi-Dirac distribution at energy ε_n. Remarkably, the shift Raman force is given in terms of the *phononic shift vector*:

$$\mathbb{R}^{mn}_{a;\ell} = [\partial_{u_a}\vartheta^{mn}_\ell + \mathbb{A}^{mm}_a - \mathbb{A}^{nn}_a]_{\mathbf{u}\to 0}\,, \tag{10}$$

with electronic velocity operator $\hat{v}_\ell = \partial_{p_\ell}\hat{H}$, whose elements can be written in polar form $v^{mn}_\ell = |v^{mn}_\ell| e^{-i\vartheta^{mn}_\ell}$, and Mead–Truhlar connection $\mathbb{A}^{nm}_a = i\langle\phi_n|\partial_{u_a}\phi_m\rangle$ [34, 35]. The phononic shift vector is invariant under independent, band-dependent $U(1)$ gauge transformations, $|\phi_n\rangle \to e^{i\theta_n(\mathbf{p},\mathbf{u})}|\phi_n\rangle$. The phononic shift vector quantifies the gauge-invariant geometric shift in the momentum conjugate to the phonon coordinate during an interband optical transition, with $\hbar\mathbb{R}$ setting the associated momentum shift, as illustrated in Fig. 1c. It encodes the geometric contribution to the impulsive lattice response generated by optically induced interband coherence and is the phononic analogue of the electronic shift vector. A numerically-accessible expression is derived in Supplementary Note 6, in terms of the interband electron–phonon coupling (EPC) matrix elements M^{mn}_a, together with $M^{mn}_{a\ell} = \langle\phi_m|\partial_{p_\ell}\hat{M}_a|\phi_n\rangle$ which is the electron–phonon–photon coupling (EPPC).

For a circularly polarized (CP) light field, the imaginary part of the QGT, corresponding to the band-resolved Berry curvature,

$$\Omega^{nm}_{bc} = -2\text{Im}[\mathcal{A}^{nm}_b \mathcal{A}^{mn}_c], \tag{11}$$

also contributes to the injection-force response. Accordingly, the CP injection force is given by

$$\alpha^{\text{inj-CP}}_{abc}(\omega) = \frac{g_s \pi e^2}{2\hbar^2} \sum_{\mathbf{p}} \sum_{mn} f_{mn} \Omega^{nm}_{bc} \Delta^{mn}_a \delta(\omega - \omega_{nm}), \tag{12}$$

and similarly the CP shift force reads

$$\beta^{\text{shi-CP}}_{abc}(\omega) = \frac{g_s \pi e^2}{4\hbar} \sum_{\mathbf{p}} \sum_{mn} f_{mn} \Big[\Omega^{mn}_{bc}\big(\mathbb{R}^{mn}_{a;+} + \mathbb{R}^{mn}_{a;-}\big) - \big(g^{mn}_{bb} + g^{mn}_{cc}\big)\big(\mathbb{R}^{mn}_{a;+} - \mathbb{R}^{mn}_{a;-}\big)\Big] \delta(\omega - \omega_{nm}), \tag{13}$$

notably depending on the *chiral phononic shift vector* $\mathbb{R}^{mn}_{a;\pm}$. This quantity is obtained from Eq. (10) by setting $\ell = \pm$ for the chiral components (with $p_\pm = \frac{p_b \pm i p_c}{\sqrt{2}}$), and it is the phononic equivalent of the chiral shift vector describing the gyration photocurrent as discussed in detail in Ref. [23]. The analytical expressions for the injection and shift-force susceptibilities in Eqs. (7)–(13) summarize the main results of this work. These expressions are not model-specific; rather they apply to generic Bloch-band Hamiltonians in which a zone-center Raman-active phonon couples to the electronic system as in Eq. (26).

Equivalent velocity- and length-gauge formulations

The quantum-geometric expressions for the injection and shift Raman forces were obtained above using the velocity gauge, where the optical field enters through the vector potential. Using a density-matrix formulation with the dipole light–matter interaction, an independent

length-gauge derivation reproduces the velocity-gauge injection and shift susceptibilities, thereby establishing their gauge invariance (see Supplementary Note 7).

In the resonant interband regime, the length-gauge calculation reproduces the same injection and shift susceptibilities obtained from the diagrammatic velocity-gauge approach. The band-diagonal EPC sector yields the injection response governed by the quantum geometric tensor and the band-resolved EPC difference, whereas the interband-coherence sector yields the shift response governed by the electronic quantum geometry weighted by the phononic shift vector. The agreement between the two formulations demonstrates that the resonant injection and shift Raman-force susceptibilities are gauge independent and that their quantum-geometric interpretation does not depend on the representation chosen for the light–matter coupling.

Conventional Raman-force theory as a limit

A useful connection with conventional descriptions of coherent-phonon generation emerges by reducing the general Raman-force response to a resonant diagonal-EPC limit. In this limit, the conventional displacive response is identified with the injection Raman force, whereas the interband-coherence channel responsible for the shift force is absent.

We take a two-band insulator with a filled valence band, v and empty conduction band, c. For light linearly polarized along $\hat{\boldsymbol{e}}_b$ and force projected along $\hat{\boldsymbol{e}}_a$, we additionally approximate the EPC difference between optically connected bands $\Delta_a^{cv} = M_a^{cc} - M_a^{vv} \simeq \overline{\Delta}_a$ as being independent of momentum. Within this system the linear electric susceptibility reads

$$\chi_{bb}^{(1)}(\omega) = \frac{g_s e^2}{\epsilon_0} \sum_{\mathbf{p}} \left[\frac{g_{bb}^{cv}}{\hbar\omega + \varepsilon_{cv} + i0^+} - \frac{g_{bb}^{cv}}{\hbar\omega - \varepsilon_{cv} + i0^+} \right], \tag{14}$$

where dielectric function, $\epsilon_{bb}(\omega) = \epsilon_0[1 + \chi_{bb}^{(1)}(\omega)]$, with ϵ_0 being the vacuum permittivity, and where ε_{cv} is the energy gap between bands. For an approximately constant gap $\varepsilon_{cv}(\mathbf{p}) \simeq \varepsilon_g$, the quantum-geometric injection response reduces to

$$\alpha_{abb}^{\mathrm{inj}}(\omega) \simeq \frac{\overline{\Delta}_a}{\varepsilon_g}\, \omega\, \mathrm{Im}\epsilon_{bb}(\omega), \tag{15}$$

and therefore the regular injection term follows as

$$\beta_{abb}^{\text{reg-inj}}(\omega) \simeq \frac{i}{2} \frac{\overline{\Delta}_a}{\varepsilon_g} \frac{d}{d\omega} \left[\omega\, \mathrm{Im}\epsilon_{bb}(\omega)\right], \tag{16}$$

Similarly, the shift response in this system can be written in terms of the dielectric function as

$$\beta_{abb}^{\mathrm{shi}}(\omega) \simeq \frac{\hbar\overline{\mathbb{R}}_{a;b}}{\varepsilon_g}\, \omega\, \mathrm{Im}\epsilon_{bb}(\omega), \tag{17}$$

with $\overline{\mathbb{R}}_{a;b}$ being the momentum-averaged interband component of the phononic shift vector, where for a two-band model with a momentum-independent EPC operator, it takes the form (see Supplementary Note 6)

$$\mathbb{R}_{a;b}^{vc} \simeq \frac{1}{\varepsilon_g}\, \mathrm{Im}\left[\frac{M_a^{vc}(v_b^{cc} - v_b^{vv})}{v_b^{vc}}\right]. \tag{18}$$

We see that nonzero interband EPC matrix elements, such as M_a^{vc}, are therefore necessary, but not sufficient, for a finite shift force, as discussed later in regard to the time reversal symmetry constraint.

Our framework recovers the conventional dielectric-function description in the reduced limit where, for the two-band insulator with momentum-independent and band-diagonal EPC, and taking the clean limit, we find (see Supplementary Note 8)

$$\chi_{abb} \simeq \frac{\overline{\Delta}_a}{\varepsilon_g} \left[\frac{\omega\, \mathrm{Im}\,\epsilon_{bb}(\omega)}{i\omega_\Sigma} - \frac{1}{2}\partial_\omega\{\omega(\epsilon_{bb}^*(\omega) - \epsilon_0)\} \right]. \tag{19}$$

The first term is the singular injection response, $\alpha_{abb}^{\mathrm{inj}}/(i\omega_\Sigma)$, which identifies the conventional displacive force with the population-driven response governed by the diagonal EPC difference. The imaginary part of the second term gives the regular injection contribution, $\beta_{abb}^{\text{reg-inj}} = (i/2)\partial_\omega \alpha_{abb}^{\mathrm{inj}}$. Its real part gives the off-resonant response, which can remain finite in the transparent subgap regime. As shown in the Supplementary Note 5, the three off-resonant contributions combine under the two-band approximation specified above as

$$\sum_{i=1}^{3} \beta_{abb}^{\mathrm{off,i}}(\omega) \simeq -\frac{\overline{\Delta}_a}{2\varepsilon_g}\partial_\omega \left[\omega\big(\mathrm{Re}\,\epsilon_{bb}(\omega) - \epsilon_0\big)\right]. \tag{20}$$

This expression recovers the conventional dispersive term $\omega\partial_\omega\, \mathrm{Re}\,\epsilon_{bb}$ and retains the additional contribution $\mathrm{Re}\,\epsilon_{bb} - \epsilon_0$. Equation (19) thus reproduces the absorptive and dispersive terms shown by Stevens *et al.* [12], while retaining the complete finite part of the expansion. Near resonance, $\hbar\omega \simeq \varepsilon_g$, the factor $\overline{\Delta}_a\omega/\varepsilon_g$ approaches $\overline{\Delta}_a/\hbar$, enabling comparison with the conventional result after matching coupling and normalization conventions.

The shift response (Eq. (17)) vanishes in this diagonal-EPC limit. It requires interband EPC and the associated electronic coherences, providing a distinct resonant impulsive contribution beyond the population-driven response. A related population-based description was developed by O'Mahony *et al.* [55], who obtain photoinduced lattice forces from nonequilibrium occupations weighted by diagonal EPC matrix elements. Such a treatment captures the population-driven physics underlying injection, whereas a description restricted to populations omits the interband coherences responsible for the shift force.

TABLE II. Symmetry properties of the resonant Raman-force susceptibility for the inversion-even Raman mode considered here under linearly polarized (LP) and circularly polarized (CP) excitation. Here, $\mathbb{R}$ and $\mathbb{R}_\pm$ denote the linear and chiral phononic shift vectors, respectively.

Sym.	$\alpha^{\text{inj-LP}}_{abc}$	$\beta^{\text{shi-LP}}_{abc}$	$\alpha^{\text{inj-CP}}_{abc}$	$\beta^{\text{shi-CP}}_{abc}$
$\mathcal{P}$	$g\otimes\Delta$: ✓	$g\otimes\mathbb{R}$: ✓	$\Omega\otimes\Delta$: ✓	$g\otimes\mathbb{R}_\pm$: ✓ $\Omega\otimes\mathbb{R}_\pm$: ✓
$\mathcal{T}$	$g\otimes\Delta$: ✓	$g\otimes\mathbb{R}$: ✗	$\Omega\otimes\Delta$: ✗	$g\otimes\mathbb{R}_\pm$: ✓ $\Omega\otimes\mathbb{R}_\pm$: ✓
$\mathcal{PT}$	$g\otimes\Delta$: ✓	$g\otimes\mathbb{R}$: ✗	$\Omega\otimes\Delta$: ✗	$g\otimes\mathbb{R}_\pm$: ✓ $\Omega\otimes\mathbb{R}_\pm$: ✗

Symmetry and polarization selection rules

The Raman force exhibits distinct symmetry characteristics relative to the second-order photocurrent [32, 33, 53]. Before evaluating the numerical values of the shift and injection Raman-force responses, we first examine their symmetry properties under parity ($\mathcal{P}$), time-reversal ($\mathcal{T}$), and combined $\mathcal{PT}$ symmetry operations. Berry curvature is odd under $\mathcal{T}$ and even under $\mathcal{P}$, whereas quantum metric is even under both $\mathcal{P}$ and $\mathcal{T}$. For the inversion-even Raman mode considered here, the phonon displacement—and consequently the EPC elements and the components of Δ^{mn}_a—are even under both $\mathcal{P}$ and $\mathcal{T}$. Additionally, the linear and chiral phononic shift vectors exhibit distinct symmetry properties: the linear phononic shift vector is *odd* under $\mathcal{T}$, while the chiral phononic shift vector changes sign and chirality under $\mathcal{T}$, that is, $\mathcal{T}\mathbb{R}_\pm\mathcal{T}^{-1} = -\mathbb{R}_\mp$. Both linear and chiral phononic shift vectors, however, are *even* under $\mathcal{P}$. The impact of $\mathcal{PT}$-symmetry emerges when $\mathcal{P}$ and $\mathcal{T}$ operations are applied concurrently. Berry curvature vanishes in $\mathcal{PT}$-symmetric contexts [21, 23], leaving only quantum metric contributions. Considering the outlined symmetries and the analytical forms presented in Eqs. (7)–(13), we summarize the main symmetry attributes of LP and CP shift and injection Raman forces within $\mathcal{P}$-, $\mathcal{T}$-, and $\mathcal{PT}$-symmetric systems in Table II. Permitted and prohibited contributions are marked with ✓ and ✗, respectively.

To illustrate these general results, we consider interlayer shear phonons in a bilayer Haldane model [56, 57], which provides a proof-of-principle model in which inversion $\mathcal{P}$ and time-reversal $\mathcal{T}$ symmetry can be controlled independently. The tight-binding Hamiltonian and electron–phonon coupling are specified in Methods.

At equilibrium, the injection and shift tensors are respectively even and odd in the $\mathcal{T}$-breaking Haldane gap δ_{H}, $\alpha^{\text{inj}}_{abc}(\omega,\delta_{\text{H}}) = \alpha^{\text{inj}}_{abc}(\omega,-\delta_{\text{H}})$ and $\beta^{\text{shi}}_{abc}(\omega,\delta_{\text{H}}) = -\beta^{\text{shi}}_{abc}(\omega,-\delta_{\text{H}})$. Combining these parities with threefold rotational symmetry and mirror covariance, under which $(x,\delta_{\text{H}}) \to (-x,-\delta_{\text{H}})$ because the Haldane mass is axial and reflection-odd, yields (see Supplementary Note 9)

$$\begin{aligned}\alpha^{\text{inj}}_{yxx} &= \alpha^{\text{inj}}_{xxy} = \alpha^{\text{inj}}_{xyx} = -\alpha^{\text{inj}}_{yyy},\\ \beta^{\text{shi}}_{xyy} &= \beta^{\text{shi}}_{yyx} = \beta^{\text{shi}}_{yxy} = -\beta^{\text{shi}}_{xxx}.\end{aligned} \tag{21}$$

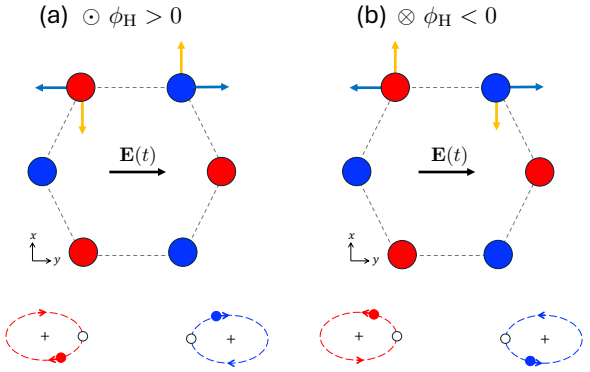

FIG. 3. Rotational motion of a zone-center E_{2g} mode driven by linearly polarized light for (a) $\phi_{\text{H}} > 0$ (⊙) and (b) $\phi_{\text{H}} < 0$ (⊗), where ϕ_{H} is the Haldane phase. Blue and gold arrows denote the displacive injection and impulsive shift forces, respectively. The perpendicular drives produce elliptical motion, becoming circular for equal oscillation amplitudes in the ideal limit of degenerate modes and negligible relaxation. Open circles mark the original equilibrium positions; crosses mark the photoinduced equilibria. The two sublattices oscillate out of phase but rotate in the same sense, which reverses when ϕ_{H} changes sign.

All remaining components vanish. All "parallel-field" components χ_{abb} are purely real at $\omega_1 + \omega_2 = 0$ due to the permutation symmetry $\chi_{abc}(\omega_1,\omega_2) = \chi_{acb}(\omega_2,\omega_1)$ and the reality condition $\chi_{abc}(\omega_1,\omega_2) = \chi^*_{abc}(-\omega_1,-\omega_2)$ [58].

A dynamical consequence of Eq. (21) is that linearly polarized light can launch rotational motion of a two-component Raman mode, as illustrated for an E_{2g} mode in Fig. 3. For a y-polarized pump, the shift and injection forces act along x and y, respectively. In the ultrashort-pulse limit, neglecting phonon damping and electronic relaxation, the ideal impulsive and displacive responses (see Fig. 2b and Ref. [12]) of initially stationary, degenerate modes yield

$$u_x(t) = u_0^{\text{shi}}\sin(\omega_p t), \quad u_y(t) = u_0^{\text{inj}}[1-\cos(\omega_p t)]. \tag{22}$$

The trajectory is elliptical about the photoinduced equilibrium $(0, u_0^{\text{inj}})$ and becomes circular when $|u_0^{\text{shi}}| = |u_0^{\text{inj}}|$. Reversing Haldane phase, ϕ_{H}, hence reversing δ_{H} reverses the shift response while preserving injection, thereby switching the sense of rotation at fixed pump polarization. Together, the directional, polarization, and reversal properties provide a more specific signature of the shift mechanism than a sine-like coherent-phonon oscillation alone. We now present the numerical results for both LP and CP injection and shift forces in this model.

Frequency and topology control of linearly polarized injection and shift forces

The numerical results for the injection and shift shear Raman-force responses to LP light (described by Eq.

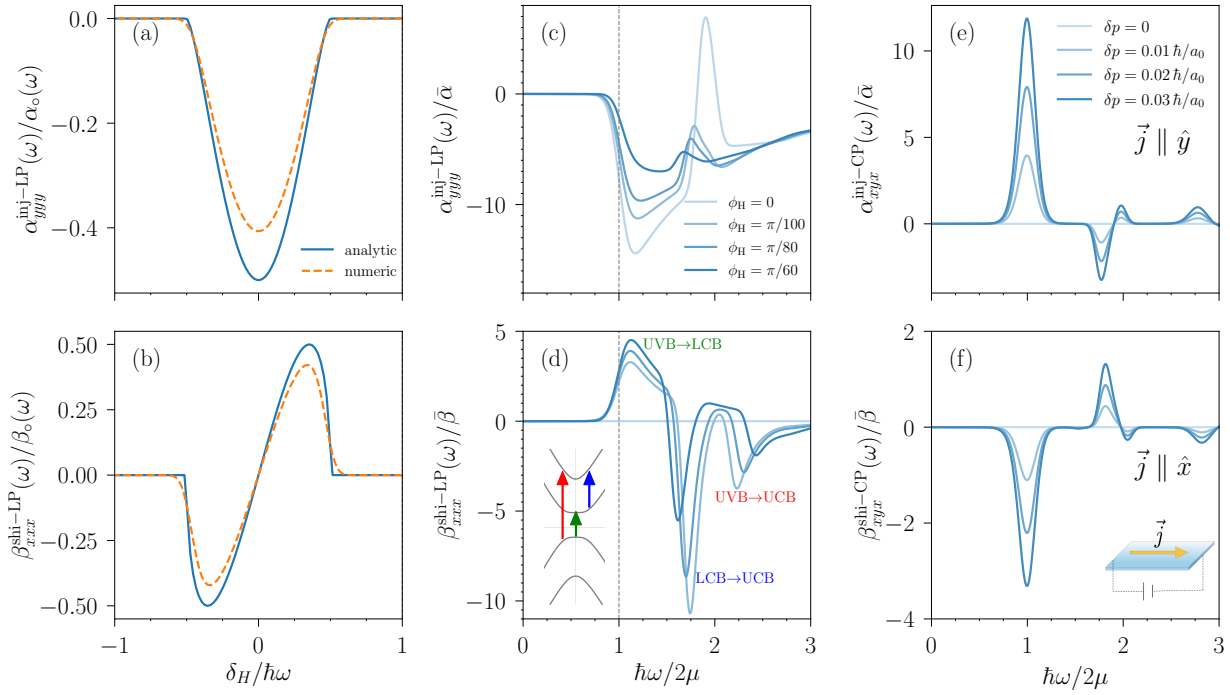

FIG. 4. Injection and shift shear Raman-force susceptibilities for linearly and circularly polarized light in the bilayer Haldane model. (a,b) LP injection and shift responses as functions of the $\mathcal{T}$-breaking Haldane gap for $\hbar\omega = 0.1$ eV, comparing analytical and numerical results and demonstrating even and odd gap dependence, respectively. (c,d) Corresponding LP spectra at $T = 50\,\mathrm{K}$ for different Haldane fluxes ϕ_{H}. The inset in (d) identifies the interband transitions responsible for the spectral features: UVB-to-LCB, LCB-to-UCB, and UVB-to-UCB. (e,f) CP injection and shift spectra at $T = 50\,\mathrm{K}$ for different current-induced momentum shifts $\delta\mathbf{p}$ of the electronic distribution. The current and momentum shift are directed along y in (e) and x in (f), as indicated. Both responses vanish at zero current and become finite when the current breaks the in-plane symmetry. We use $\phi_{\mathrm{H}} = 0$ in (e), $\phi_{\mathrm{H}} = \pi/80$ in (f), and a sublattice potential $\delta = 0.05\,\mathrm{eV}$ in both panels. We set chemical potential, $\mu = 0.1$ eV throughout, which is within the LCB. The normalization factors are $\alpha_\circ(\omega) = e^2\mathcal{M}/(\hbar^2\omega)$, $\beta_\circ(\omega) = e^2\mathcal{M}/(\hbar\omega)^2$, $\bar{\alpha} = 100\,\mathrm{nN/(V^2\,ps)}$, and $\bar{\beta} = 1\,\mathrm{nN/V^2}$. The model parameters are $\gamma_0 = 3.16\,\mathrm{eV}$, $\gamma_1 = 0.381\,\mathrm{eV}$, and $\gamma_3 = 0.38\,\mathrm{eV}$ [59]; $\gamma' = 0.3\,\mathrm{eV}$ [60]; and $a_0 = 1.42\,\text{Å}$, $b = 2.59\,\text{Å}$, and $\beta_3 = 5.24$ [61].

(7)) in the bilayer Haldane model are depicted in Fig. 4. In panels (a) and (b), we show the injection and shift responses as functions of the $\mathcal{T}$-breaking Haldane gap, scaled to the light frequency, $\hbar\omega$. As seen, the injection force is largest in the gapless regime and diminishes as the Haldane gap increases. It retains the same sign for both positive and negative values of the Haldane gap. On the other hand, panel (b) displays the shift response, which shows an odd-parity dependence on the Haldane gap: it vanishes in the gapless regime (corresponding to the $\mathcal{T}$-symmetric case) as expected from above, rises, and then falls again as the Haldane gap increases.

We analyze the system using a low-energy $\mathbf{k}\cdot\mathbf{p}$ model near the hexagonal Brillouin zone corners (valleys $\tau = \pm$), defined by $\mathcal{H} = -p^2(\cos 2\varphi\hat{\sigma}_x + \tau\sin 2\varphi\hat{\sigma}_y)/2m - \tau\delta_{\mathrm{H}}\hat{\sigma}_z$, where φ is the polar angle of momentum $\mathbf{p}$. Here, Pauli matrices represent the layer pseudo-spin, $m = 2\hbar^2\gamma_1/9\gamma_0^2a_0^2$, and δ_{H} denotes the Haldane gap. Moreover, close to the valley point, the EPC reads $(M_x, M_y) = \mathcal{M}(\tau\hat{\sigma}_y, \hat{\sigma}_x)$, with $\mathcal{M} = 3a_0\gamma_3\beta_3/\sqrt{2}b^2$ being the electron coupling constant to shear phonons. Using the two-band model, we analytically evaluate the relevant quantum-geometric quantities (see Methods) and obtain the injection and shift Raman-force responses for linearly polarized excitation:

$$\alpha^{\mathrm{inj-LP}}_{yyy} = -4\alpha_\circ(\omega)\left(1/4 - z^2\right)^{3/2}\Theta\left(1/2 - |z|\right), \quad (23)$$

$$\beta^{\mathrm{shi-LP}}_{xxx} = +4\beta_\circ(\omega)z\left(1/4 - z^2\right)^{1/2}\Theta\left(1/2 - |z|\right), \quad (24)$$

where $z = \delta_{\mathrm{H}}/\hbar\omega$, $\Theta(\dots)$ is the Heaviside step function, and by including the spin degeneracy factor, we have $\alpha_\circ(\omega) = e^2\mathcal{M}/\hbar^2\omega$ and $\beta_\circ(\omega) = e^2\mathcal{M}/(\hbar\omega)^2$. These analytical results are compared with full Brillouin zone numerical calculations from the four-band model, as shown in Fig. 4a,b. The two-band model reproduces the qualitative dependence of the full four-band calculation, while quantitative differences likely arise from trigonal warping and multiband transitions present in the full tight-binding model.

To further investigate the effect of multiband transitions, we compute the injection and shift response functions as a function of light frequency scaled by 2μ. As shown in Fig. 4c, in the absence of magnetic flux ($\phi_{\mathrm{H}} = 0$), corresponding to standard bilayer graphene, the injec-

tion response susceptibility $\alpha^{\text{inj-LP}}_{yyy}$ is finite and exhibits a step at the interband optical gap $\hbar\omega = 2\mu$, associated with transitions between the upper valence band (UVB) and lower conduction band (LCB). At higher frequencies, a peak emerges due to transitions from the LCB to the upper conduction band (UCB). Notably, this transition induces a π-phase (direction) shift in the injection force, revealing a strong frequency dependence in the phase of coherent phonon oscillations and the direction of the rectified displacement. As magnetic flux ϕ_{H} is introduced and increased, a Haldane gap opens between the UVB and LCB, resulting in a reduced step height in the low-frequency response, consistent with the trend shown in panel (a). Similarly, Fig. 4d depicts the shift response as a function of frequency. The response shows an interband transition step corresponding to transitions from the UVB to LCB. The step height increases from zero to a finite value and exhibits an increasing trend with increasing magnetic flux, consistent with Fig. 4b. At higher energies, additional spectral features arise from LCB-to-UCB and UVB-to-UCB transitions (with LVB-to-LCB contributions yielding a subdominant response), with the former producing the pronounced sign-changing feature near the split-band threshold. The corresponding UVB-to-UCB feature is considerably weaker in the injection response and does not appear as a distinct spectral feature.

Hot-electron effects are generally unavoidable in nonlinear optical experiments on small-gap materials, and they can significantly modify the Raman-force response through the temperature dependence of the electronic occupations. We therefore analyze the effect of electronic temperature on the LP Raman force in Supplementary Note 10. The main effect is not simply thermal broadening: increasing temperature redistributes carriers between valence and conduction bands and shifts the chemical potential downward at fixed carrier density. These changes reduce Pauli blocking near the low-energy absorption edge, activate transitions closer to the Haldane gap, and modify the relative weight of UVB-to-LCB, LCB-to-UCB, and LVB-to-UVB transitions. As a result, the LP injection and shift forces acquire a pronounced temperature dependence, with the injection response enhanced by thermally activated conduction-band transitions, while the shift response reflects a competition between population spreading and the temperature-induced shift of the chemical potential. These effects are shown in Supplementary Fig. 3.

Current-induced circular Raman forces from Fermi-surface symmetry breaking

Here, we discuss the resonant Raman shear-force response to circularly polarized (CP) light. This is motivated by the growing interest in optically exciting coherent chiral or axial phonons and controlling phonon angular momentum with circularly polarized light fields [62].

For the second-order force response in Eq. (2), the susceptibility can be decomposed into components that are symmetric and antisymmetric under exchange of the two optical indices, $\chi^{\text{S/A}}_{abc} = \frac{1}{2}(\chi_{abc} \pm \chi_{acb})$. The symmetric part governs the LP-response, while the antisymmetric part governs the CP-response, with the relevant circular component in two dimensions given by χ^{A}_{axy}. Using intrinsic permutation symmetry, $\chi_{abc}(\omega_1, \omega_2) = \chi_{acb}(\omega_2, \omega_1)$, and the reality condition, $\chi_{abc}(\omega_1, \omega_2) = \chi^*_{abc}(-\omega_1, -\omega_2)$ [58], the rectified CP response satisfies $\chi^{\text{A}}_{axy}(\omega, -\omega) = i\,\text{Im}\,\chi_{axy}(\omega, -\omega)$. Therefore, the CP Raman force is governed by the imaginary, antisymmetric part of the rectified Raman susceptibility, in direct analogy with helicity-dependent nonlinear photocurrents [23], with the corresponding resonant CP injection and shift susceptibilities given by Eqs. (12) and (13).

For the equilibrium bilayer Haldane model, the CP Raman shear-force response vanishes despite the finite Haldane flux because threefold rotational symmetry remains intact. This is because of the symmetry constraints outlined in Eq. (21), which enforce χ_{axy} to be real, thus making its antisymmetric (circular) component vanish. A finite CP Raman shear force therefore requires breaking C_3 symmetry. A source–drain dc current provides a natural route by producing a stationary drift distortion of the electronic distribution that selects an in-plane direction. We model this drift by a momentum-shifted Fermi distribution,

$$f^{\text{neq}}_m(\mathbf{p}) = f_m(\mathbf{p} + \delta\mathbf{p}), \qquad \delta\mathbf{p} = e\tau\mathbf{E}_{\text{dc}}, \tag{25}$$

where $\tau = 1/\Gamma$ is the intraband transport relaxation time and $\mathbf{E}_{\text{dc}}$ is the static bias electric field. The current-induced distortion, $\delta f_m(\mathbf{p}) = f^{\text{neq}}_m(\mathbf{p}) - f_m(\mathbf{p})$, reduces in the small-shift limit to $\delta f_m(\mathbf{p}) \simeq \delta\mathbf{p} \cdot \nabla_{\mathbf{p}} f_m(\mathbf{p})$. Since $\delta\mathbf{p}$ changes sign under both $\mathcal{T}$ and $\mathcal{P}$, a finite drift shift breaks the corresponding equilibrium symmetries and allows response components forbidden in the equilibrium case summarized in Table II.

The resulting CP spectra are shown in Fig. 4e,f for both shift and injection channels. At $\delta p = 0$, both CP responses vanish, as required by symmetry. For finite δp, the responses become nonzero and increase with the magnitude of the current-induced distribution shift. Since the current-induced occupation change δf_m is concentrated near the Fermi surface at low temperature, the CP Raman force is dominated by optical transitions involving the partially occupied low-energy conduction band (LCB) containing the Fermi level. As a result, the CP response is highly sensitive to current-induced distortions of the Fermi surface. This contrasts with the LP response, which is already symmetry-allowed in equilibrium and therefore does not rely on such nonequilibrium Fermi-surface distortions.

Three spectral features appear in both CP injection and shift shear Raman forces in Fig. 3e,f: a UVB-to-LCB resonance at $\hbar\omega = 2\mu$, a sign-changing LCB-to-UCB resonance, and a weaker LVB-to-LCB resonance. All three features are Fermi-surface effects involving transitions to

or from the LCB, as expected. The sign change of the LCB-to-UCB resonance relative to the other two spectral features reflects the variation of the relevant interband EPC matrix element over the momentum shell sampled across the transition threshold.

CONCLUSION

Taken together, the quantum-geometric decomposition, its gauge-invariant formulation, and the recovery of the conventional dielectric-function limit establish a unified picture of rectified Raman forces. Within this picture, the resonant response separates into two mechanisms with distinct microscopic origins and temporal dynamics. The conventional displacive force is identified with the injection contribution and is governed by the quantum geometric tensor together with the band-resolved asymmetry of the diagonal EPC. The shift force, by contrast, originates from interband EPC and electronic coherences and provides a distinct impulsive mechanism in the absorbing regime governed by the quantum geometric tensor and the phononic shift vector.

The polarization dependence is strongly constrained by time-reversal symmetry. For LP excitation, the injection force is allowed in a time-reversal-symmetric system, whereas the shift force vanishes and requires broken time-reversal symmetry. For CP excitation, the injection force vanishes under time reversal, while the shift force can remain finite. Thus, in a time-reversal-symmetric system, circularly polarized light provides a direct route to generating the resonant shift Raman force without magnetic time-reversal-symmetry breaking, provided that the relevant response is allowed by crystalline symmetry.

For the bilayer system considered here, these mechanisms provide distinct routes to coherently control interlayer shear motion. Their magnitude and direction can be controlled through the optical frequency and Haldane flux, while circularly polarized responses can additionally be activated through current-induced Fermi-surface symmetry breaking. Their temporal signatures are also qualitatively different: the injection contribution produces a displacive force that persists on the electronic relaxation timescale, whereas the shift contribution acts impulsively during the optical pulse, as illustrated in Fig. 2.

Experimentally, these dynamics can be probed through coherent phonon displacements in pump–probe measurements [13], including time-resolved reflectivity [4, 8, 39], second-harmonic generation [41, 63], Raman spectroscopy [64], coherent band shifts in time-resolved ARPES [65, 66], and Bragg-peak intensity changes in electron or x-ray diffraction [3, 67]. Substrate effects can be reduced through lattice mismatch, free suspension [37], or by studying bulk layered materials. In time-resolved reflectivity [8], for example, the differential signal follows the coherent displacement, $\Delta R(t)/R \propto u(t)$, providing a direct route to distinguishing the displacive injection and impulsive shift dynamics.

Our results therefore extend quantum geometry from electronic transport and optical response to the generation and control of coherent lattice motion, providing a quantum-geometric route toward light-induced phase control in quantum materials. Coherent-phonon amplitudes, phases, polarization dependence, and temporal dynamics thereby offer experimentally accessible signatures of the quantum metric, Berry curvature, and electron–phonon geometric quantities such as the phononic shift vector.

METHODS

Kadanoff–Baym Raman-force formalism

We consider a generic electronic Bloch Hamiltonian coupled to a zone-center Raman-active phonon displacement $\mathbf{u}$ with frequency ω_p. Expanding the electronic Hamiltonian to linear order in the phonon displacement, we write [68]

$$\hat{\mathcal{H}} = \sum_{\mathbf{p}} \hat{\psi}^{\dagger}_{\mathbf{p}} \left[\hat{H}(\mathbf{p}) + \hat{\mathbf{M}}(\mathbf{p}) \cdot \mathbf{u} \right] \hat{\psi}_{\mathbf{p}}, \tag{26}$$

where $\hat{H}(\mathbf{p})$ is the equilibrium electronic Bloch Hamiltonian and

$$\hat{M}_a(\mathbf{p}) = \left. \frac{\partial \hat{H}(\mathbf{p}, \mathbf{u})}{\partial u_a} \right|_{\mathbf{u}=0} \tag{27}$$

is the electron–phonon coupling (EPC) operator associated with the phonon coordinate u_a. The electronic field operator at momentum $\mathbf{p}$ is denoted by $\hat{\psi}_{\mathbf{p}}$. The light–matter interaction Hamiltonian is obtained by coupling light to the electrons via the minimal coupling substitution $\mathbf{p} \to \mathbf{p} + e\mathbf{A}(t)$, where $\mathbf{A}(t)$ is a homogeneous vector potential. Here, we focus on the electron-mediated Raman force and neglect direct ionic coupling to the optical field. Four relevant light–matter couplings are given by $\partial_{p_a}\hat{H}$, $\partial_{p_a}\partial_{p_b}\hat{H}$, $\partial_{p_b}\hat{M}_a$, and $\partial_{p_c}\partial_{p_b}\hat{M}_a$, corresponding respectively to one-photon, two-photon, one-photon–phonon, and two-photon–phonon couplings [69].

Using the Kadanoff–Baym variational formalism [70–72] (summarized below; full derivation in Supplementary Note 1), we derive the Raman force perturbatively to second order in the electric field. The susceptibility χ_{abc} contains resonant injection and shift contributions together with three off-resonant contributions. The complete set of diagrams is shown in Supplementary Fig. 1, while Fig. 5 shows the triangle and oval diagrams that contain the resonant terms. The formal evaluation of these contributions in the band basis and their quantum-geometric decomposition are presented in Supplementary Note 2 and Supplementary Note 3, respectively.

In the band basis, the triangle diagram yields the singular injection response, its regular correction, a first off-resonant contribution, $\beta^{\mathrm{off},1}_{abc}$, and a counterterm, γ^{Δ}_{abc}.

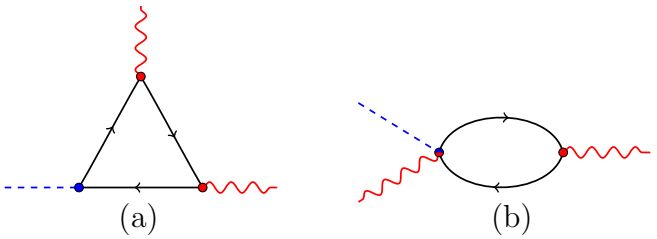

FIG. 5. Feynman diagrams contributing to the resonant Raman-force response. Solid, dashed, and wavy lines denote electron, phonon, and photon propagators, respectively. Red, blue, and combined red-blue vertices represent velocity, electron–phonon, and mixed electron–phonon–photon couplings. (a) The triangle diagram yields the singular and regular injection contributions, an off-resonant term, and a counterterm. (b) The oval diagram yields the shift contribution, a second off-resonant term, and the opposite counterterm. The counterterms cancel in the clean, noninteracting limit.

The oval diagram yields the resonant shift force, $\beta^{\rm shi}_{abc}$; a second off-resonant contribution, $\beta^{\rm off,2}_{abc}$, which remains finite in the transparent regime; and a counterterm, $\gamma^{\rm O}_{abc}$. The latter is equal in magnitude and opposite in sign to the triangle-diagram counterterm γ^{Δ}_{abc}, so that in the clean, noninteracting limit

$$\gamma^{\Delta}_{abc} + \gamma^{\rm O}_{abc} = 0. \tag{28}$$

A detailed proof of this cancellation is provided in Supplementary Note 4.

Shear phonons in a bilayer Haldane model

Having developed the Raman-force formalism for a generic multiband Bloch Hamiltonian, we now specialize to a two-dimensional bilayer Haldane model and its interlayer shear phonon.

We quantitatively compute the injection and shift forces that excite interlayer shear modes in a bilayer system. To incorporate $\mathcal{P}$- and $\mathcal{T}$-symmetry breaking, we analyze injection and shift responses in the bilayer Haldane model [56, 57], which breaks $\mathcal{T}$-symmetry via magnetic flux and $\mathcal{P}$-symmetry via sublattice staggering. We employ a four-band Hamiltonian with hexagonal symmetry, where block-diagonal terms describe an individual Haldane model [56] in each layer with flux $\phi_{\rm H}$, as given by

$$\hat{\mathcal{H}} = \hat{H}_H \otimes \hat{\tau}_0 + \hat{H}_{12} \otimes \hat{\tau}_- + \hat{H}^\dagger_{12} \otimes \hat{\tau}_+, \tag{29}$$

where $\hat{\tau}_i$ and $\hat{\sigma}_i$ $(i = x, y, z)$ are Pauli matrices in layer and sublattice space, $\hat{\tau}_\pm = (\hat{\tau}_x \pm i\hat{\tau}_y)/2$, $\hat{\sigma}_\pm = (\hat{\sigma}_x \pm i\hat{\sigma}_y)/2$, $\hat{H}_H = d_0\hat{\sigma}_0 + \mathbf{d}\cdot\hat{\boldsymbol{\sigma}}$, with

$$\begin{aligned} d_0 &= -2\gamma' \cos\phi_{\rm H}\,(\mathrm{Re}[\zeta_{\mathbf{p}}] + 3/2)\,, \\ d_x - id_y &= -\gamma_0 \xi_{\mathbf{p}}, \\ d_z &= \delta + 2\gamma' \sin\phi_{\rm H}\ \mathrm{Im}[\zeta_{\mathbf{p}}]. \end{aligned} \tag{30}$$

The interlayer term is $\hat{H}_{12} = \gamma_1\hat{\sigma}_+ - \gamma_3\xi_{\mathbf{p}}\hat{\sigma}_-$. Here, the nearest and next-nearest neighbor form factors are

$$\xi_{\mathbf{p}} = e^{ip_y} + 2e^{-ip_y/2}\cos\left(\sqrt{3}p_x/2\right), \tag{31}$$

$$\zeta_{\mathbf{p}} = e^{i\sqrt{3}p_x} + 2e^{-i\sqrt{3}p_x/2}\cos\left(3p_y/2\right). \tag{32}$$

Note that $\mathbf{p}$ is measured in units of $\hbar/a_0$. The parameters γ_0 and γ' describe the nearest and next-nearest neighbor intralayer hopping energies, while γ_1 and γ_3 correspond to the interlayer hopping terms [73]. The parameter δ represents the sublattice symmetry-breaking term that opens a trivial gap and breaks $\mathcal{P}$ symmetry, while the Haldane magnetic flux $\phi_{\rm H}$ generates the $\mathcal{T}$-breaking Haldane mass $\delta_{\rm H} = 3\sqrt{3}\gamma'\sin\phi_{\rm H}$, corresponding to a gap $2|\delta_{\rm H}|$ when $\delta = 0$. Since $\phi_{\rm H}$ affects only intralayer hopping phases, the interlayer EPC is the same as in Bernal-stacked bilayer graphene [61], namely

$$\hat{\mathbf{M}} = \hat{M}_{12}\otimes\tau_- + \hat{M}^\dagger_{12}\otimes\tau_+, \quad \hat{M}_{12} = -i\hbar\mathcal{C}\partial_{\mathbf{p}}\xi_{\mathbf{p}}\,\sigma_-, \tag{33}$$

where $\mathcal{C} = \sqrt{2}\gamma_3\beta_3/b^2$, with Grüneisen parameter, $\beta_3 = -\partial\ln\gamma_3/\partial\ln b$ quantifying the strength of the EPC, and b the interatomic distance for γ_3-hopping.

Projecting the four-band model onto its low-energy two-band sector allows us to obtain analytical expressions for the relevant quantum-geometric quantities. We find

$$\boldsymbol{\Delta}^{cv} = -2\mathcal{M}(1+X^2)^{-1/2}\,(\sin 2\varphi,\ \cos 2\varphi), \tag{34}$$

$$\mathbf{g}^{cv} = \frac{\hbar^2}{p^2(1+X^2)^2}\begin{bmatrix} X_s^2(\varphi) & -\frac{1}{2}\sin 2\varphi \\ -\frac{1}{2}\sin 2\varphi & X_c^2(\varphi)\end{bmatrix}, \tag{35}$$

and

$$\mathbb{R}^{cv} = \frac{\mathcal{M}X}{\epsilon_p\sqrt{1+X^2}}\begin{bmatrix} -\cos^2\varphi/X_s^2(\varphi) & \sin^2\varphi/X_c^2(\varphi) \\ \sin 2\varphi/2X_s^2(\varphi) & \sin 2\varphi/2X_c^2(\varphi)\end{bmatrix}, \tag{36}$$

where $X = \delta_{\rm H}/\epsilon_p$ with $\epsilon_p = p^2/2m$, $X_s^2(\varphi) = X^2 + \sin^2\varphi$, and $X_c^2(\varphi) = X^2 + \cos^2\varphi$. From the φ-dependence of the Cartesian components of $\boldsymbol{\Delta}^{cv}$, $\mathbf{g}^{cv}$, and $\mathbb{R}^{cv}$, we see that the non-vanishing injection and shift components obey Eq. (21). Moreover, for small $X \ll 1$, the shift vector rises linearly with X, whereas for larger $X \gg 1$, it diminishes with increasing magnetic flux. Substituting the quantum-geometric quantities derived above yields the analytical LP injection- and shift-force susceptibilities given in Eqs. (23) and (24), respectively.

ACKNOWLEDGMENTS

We acknowledge support from the Engineering and Physical Sciences Research Council (Grant No. UKRI122) and the Royal Society (Grant No. IES\R2\242309). We thank R. Stanier, S. Patel, E. Da Como, D. Wolverson, S. Bending, E. Cappelluti, N. Nagaosa and L. Benfatto for helpful comments.

CORRESPONDENCE

Habib Rostami (hr745@bath.ac.uk)

AUTHOR CONTRIBUTIONS

H.R. conceived and supervised the project. J.L.P. carried out the analytical and numerical calculations. J.L.P. and H.R. developed the theoretical framework, analyzed the results, and wrote and revised the manuscript.

DATA AVAILABILITY

The data supporting the findings of this study are available from the corresponding author upon reasonable request.

CODE AVAILABILITY

The custom code used to generate the numerical results and figures is available from the corresponding author upon reasonable request.

COMPETING INTERESTS

The authors declare no competing interests.

[1] A. S. Disa, T. F. Nova, and A. Cavalleri, Nature Physics **17**, 1087 (2021).
[2] A. de la Torre, D. M. Kennes, M. Claassen, S. Gerber, J. W. McIver, and M. A. Sentef, Rev. Mod. Phys. **93**, 041002 (2021).
[3] E. J. Sie, C. M. Nyby, C. D. Pemmaraju, S. J. Park, X. Shen, J. Yang, M. C. Hoffmann, B. K. Ofori-Okai, R. Li, A. H. Reid, S. Weathersby, E. Mannebach, N. Finney, D. Rhodes, D. Chenet, A. Antony, L. Balicas, J. Hone, T. P. Devereaux, T. F. Heinz, X. Wang, and A. M. Lindenberg, Nature **565**, 61 (2019).
[4] D. Soranzio, M. Peressi, R. J. Cava, F. Parmigiani, and F. Cilento, Phys. Rev. Res. **1**, 032033 (2019).
[5] M. Basini, M. Pancaldi, B. Wehinger, M. Udina, V. Unikandanunni, T. Tadano, M. C. Hoffmann, A. V. Balatsky, and S. Bonetti, Nature **628**, 534 (2024).
[6] Y. Okamura, T. Morimoto, N. Ogawa, Y. Kaneko, G.-Y. Guo, M. Nakamura, M. Kawasaki, N. Nagaosa, Y. Tokura, and Y. Takahashi, Proceedings of the National Academy of Sciences **119**, e2122313119 (2022).
[7] B. Huang, S. Li, B. Li, Y. Shan, J. Cheng, H. Chen, J. Liu, and X. Xie, Applied Physics Letters **127**, 082101 (2025).
[8] H. J. Zeiger, J. Vidal, T. K. Cheng, E. P. Ippen, G. Dresselhaus, and M. S. Dresselhaus, Phys. Rev. B **45**, 768 (1992).
[9] L. Dhar, J. A. Rogers, and K. A. Nelson, Chemical Reviews **94**, 157 (1994).
[10] G. A. Garrett, T. F. Albrecht, J. F. Whitaker, and R. Merlin, Phys. Rev. Lett. **77**, 3661 (1996).
[11] R. Merlin, Solid State Communications **102**, 207 (1997).
[12] T. E. Stevens, J. Kuhl, and R. Merlin, Phys. Rev. B **65**, 144304 (2002).
[13] M. Udina, T. Cea, and L. Benfatto, Phys. Rev. B **100**, 165131 (2019).
[14] H. Rostami, Phys. Rev. B **106**, 155405 (2022).
[15] H. Rostami, Phys. Rev. B **107**, 165418 (2023).
[16] J. P. Provost and G. G. Vallee, Commun. Math. Phys. **76**, 289 (1980).
[17] M. V. Berry, Proc. R. Soc. **392**, 45 (1984).
[18] P. Törmä, S. Peotta, and B. A. Bernevig, Nature Reviews Physics **4**, 528 (2022).
[19] N. Nagaosa, J. Sinova, S. Onoda, A. H. MacDonald, and N. P. Ong, Rev. Mod. Phys. **82**, 1539 (2010).
[20] S. Peotta and P. Törmä, Nature Communications **6**, 8944 (2015).
[21] T. Holder, D. Kaplan, and B. Yan, Phys. Rev. Res. **2**, 033100 (2020).
[22] J. Ahn, G.-Y. Guo, and N. Nagaosa, Phys. Rev. X **10**, 041041 (2020).
[23] H. Watanabe and Y. Yanase, Phys. Rev. X **11**, 011001 (2021).
[24] A. Agarwal, W. Jankowski, D. Bennett, and R.-J. Slager, npj 2D Materials and Applications **9**, 43 (2025).
[25] C. Wang, Y. Gao, and D. Xiao, Phys. Rev. Lett. **127**, 277201 (2021).
[26] N. Wang, D. Kaplan, Z. Zhang, T. Holder, N. Cao, A. Wang, X. Zhou, F. Zhou, Z. Jiang, C. Zhang, S. Ru, H. Cai, K. Watanabe, T. Taniguchi, B. Yan, and W. Gao, Nature **621**, 487 (2023).
[27] A. Gao, Y.-F. Liu, J.-X. Qiu, B. Ghosh, T. V. Trevisan, Y. Onishi, C. Hu, T. Qian, H.-J. Tien, S.-W. Chen, M. Huang, D. Bérubé, H. Li, C. Tzschaschel, T. Dinh, Z. Sun, S.-C. Ho, S.-W. Lien, B. Singh, K. Watanabe, T. Taniguchi, D. C. Bell, H. Lin, T.-R. Chang, C. R. Du, A. Bansil, L. Fu, N. Ni, P. P. Orth, Q. Ma, and S.-Y. Xu, Science **381**, 181 (2023).
[28] J. Yu, C. J. Ciccarino, R. Bianco, I. Errea, P. Narang, and B. A. Bernevig, Nature Physics **20**, 1262 (2024).
[29] J. Hu, Z. Zhu, Y. Yuan, H. Wang, and K. Chang, Phys. Rev. Lett. **135**, 256405 (2025).
[30] J. Hu, W. Li, Z. Guo, H. Wang, and K. Chang, Phys. Rev. Lett. **135**, 256404 (2025).
[31] G. Pellitteri, Z. Dai, H. Hu, Y. Jiang, G. Menichetti, A. Tomadin, B. A. Bernevig, and M. Polini, Phys. Rev. B **112**, 245128 (2025).
[32] J. E. Sipe and A. I. Shkrebtii, Phys. Rev. B **61**, 5337 (2000).
[33] S. M. Young and A. M. Rappe, Phys. Rev. Lett. **109**, 116601 (2012).

[34] C. A. Mead and D. G. Truhlar, The Journal of Chemical Physics **70**, 2284 (1979).
[35] R. Resta, Journal of Physics: Condensed Matter **12**, R107 (2000).
[36] P. H. Tan, W. P. Han, W. J. Zhao, Z. H. Wu, K. Chang, H. Wang, Y. F. Wang, N. Bonini, N. Marzari, N. Pugno, G. Savini, A. Lombardo, and A. C. Ferrari, Nature Materials **11**, 294 (2012).
[37] D. Boschetto, L. Malard, C. H. Lui, K. F. Mak, Z. Li, H. Yan, and T. F. Heinz, Nano Letters **13**, 4620 (2013).
[38] Y. Zhao, X. Luo, H. Li, J. Zhang, P. T. Araujo, C. K. Gan, J. Wu, H. Zhang, S. Y. Quek, M. S. Dresselhaus, and Q. Xiong, Nano Letters **13**, 1007 (2013).
[39] F. M. Bartram, Y.-C. Leng, Y. Wang, L. Liu, X. Chen, H. Peng, H. Li, P. Yu, Y. Wu, M.-L. Lin, J. Zhang, P.-H. Tan, and L. Yang, npj Quantum Materials **7**, 84 (2022).
[40] J. Zhang, J. Han, G. Peng, X. Yang, X. Yuan, Y. Li, J. Chen, W. Xu, K. Liu, Z. Zhu, W. Cao, Z. Han, J. Dai, M. Zhu, S. Qin, and K. S. Novoselov, Light: Science & Applications **9**, 174 (2020).
[41] M. Y. Zhang, Z. X. Wang, Y. N. Li, L. Y. Shi, D. Wu, T. Lin, S. J. Zhang, Y. Q. Liu, Q. M. Liu, J. Wang, T. Dong, and N. L. Wang, Phys. Rev. X **9**, 021036 (2019).
[42] T. Fukuda, K. Makino, Y. Saito, P. Fons, A. V. Kolobov, K. Ueno, and M. Hase, Applied Physics Letters **116**, 093103 (2020).
[43] M. Rodriguez-Vega, Z.-X. Lin, A. Leonardo, A. Ernst, M. G. Vergniory, and G. A. Fiete, J. Phys. Chem. Lett. **13**, 4152 (2022).
[44] H. Zhong, S. Yang, C. Cao, X.-Y. Feng, and J. Dai, Phys. Rev. B **113**, 075111 (2026).
[45] Q. Yang and S. Meng, Phys. Rev. Lett. **133**, 136902 (2024).
[46] K. Yasuda, E. Zalys-Geller, X. Wang, D. Bennett, S. S. Cheema, K. Watanabe, T. Taniguchi, E. Kaxiras, P. Jarillo-Herrero, and R. Ashoori, Science **385**, 53 (2024).
[47] X. Wang, K. Yasuda, Y. Zhang, S. Liu, K. Watanabe, T. Taniguchi, J. Hone, L. Fu, and P. Jarillo-Herrero, Nature Nanotechnology **17**, 367 (2022).
[48] R. Bian, R. He, E. Pan, Z. Li, G. Cao, P. Meng, J. Chen, Q. Liu, Z. Zhong, W. Li, and F. Liu, Science **385**, 57 (2024).
[49] X. Sun, Q. Xia, T. Cao, and S. Yuan, Materials Science and Engineering: R: Reports **163**, 100927 (2025).
[50] W. Qin and A. H. MacDonald, Phys. Rev. Lett. **127**, 097001 (2021).
[51] F. de Juan, A. G. Grushin, T. Morimoto, and J. E. Moore, Nature Communications **8**, 15995 (2017).
[52] N. Laman, M. Bieler, and H. M. van Driel, Journal of Applied Physics **98**, 103507 (2005).
[53] R. von Baltz and W. Kraut, Phys. Rev. B **23**, 5590 (1981).
[54] F. Nastos and J. E. Sipe, Phys. Rev. B **74**, 035201 (2006).
[55] S. M. O'Mahony, F. Murphy-Armando, E. D. Murray, J. D. Querales-Flores, I. Savić, and S. Fahy, Phys. Rev. Lett. **123**, 087401 (2019).
[56] F. D. M. Haldane, Phys. Rev. Lett. **61**, 2015 (1988).
[57] S. Sorn, Phys. Rev. B **98**, 125145 (2018).
[58] P. N. Butcher and D. Cotter, *The elements of nonlinear optics* (Cambridge university press, 1990).
[59] A. B. Kuzmenko, I. Crassee, D. van der Marel, P. Blake, and K. S. Novoselov, Phys. Rev. B **80**, 165406 (2009).
[60] N. M. R. Peres, F. Guinea, and A. H. Castro Neto, Phys. Rev. B **73**, 125411 (2006).
[61] E. Cappelluti and G. Profeta, Phys. Rev. B **85**, 205436 (2012).
[62] D. M. Juraschek, R. M. Geilhufe, H. Zhu, M. Basini, P. Baum, A. Baydin, S. Chaudhary, M. Fechner, B. Flebus, G. Grissonnanche, A. I. Kirilyuk, M. Lemeshko, S. F. Maehrlein, M. Mignolet, S. Murakami, Q. Niu, U. Nowak, C. P. Romao, H. Rostami, T. Satoh, N. A. Spaldin, H. Ueda, and L. Zhang, Nature Physics **21**, 1532 (2025).
[63] R. Mankowsky, A. von Hoegen, M. Först, and A. Cavalleri, Phys. Rev. Lett. **118**, 197601 (2017).
[64] H. Kuramochi and T. Tahara, Journal of the American Chemical Society **143**, 9699 (2021).
[65] X. Shi, W. You, Y. Zhang, Z. Tao, P. M. Oppeneer, X. Wu, R. Thomale, K. Rossnagel, M. Bauer, H. Kapteyn, and M. Murnane, Science Advances **5**, eaav4449 (2019).
[66] C. J. Sayers, G. Cerullo, Y. Zhang, C. E. Sanders, R. T. Chapman, A. S. Wyatt, G. Chatterjee, E. Springate, D. Wolverson, E. Da Como, and E. Carpene, Phys. Rev. Lett. **130**, 156401 (2023).
[67] D. Soranzio, M. Savoini, P. Beaud, F. Cilento, L. Boie, J. Dössegger, V. Ovuka, S. Houver, M. Sander, S. Zerdane, E. Abreu, Y. Deng, R. Mankowsky, H. T. Lemke, F. Parmigiani, M. Peressi, and S. L. Johnson, npj 2D Materials and Applications **6**, 71 (2022).
[68] F. Giustino, Rev. Mod. Phys. **89**, 015003 (2017).
[69] D. M. Basko, New Journal of Physics **11**, 095011 (2009).
[70] G. Baym and L. P. Kadanoff, Phys. Rev. **124**, 287 (1961).
[71] L. P. Kadanoff and G. Baym, *Quantum Statistical Mechanics* (W. A. Benjamin, Inc., 1962).
[72] H. Rostami and E. Cappelluti, npj 2D Materials and Applications **5**, 50 (2021).
[73] E. McCann and M. Koshino, Rep. Prog. Phys. **76**, 056053 (2013).

Supplementary Files

This is a list of supplementary files associated with this preprint. Click to download.

- SIRamanForcecommphys.pdf